Experimental evidence of the effect of solute concentration on the collective evolution of bubbles in a regular pore-network

Joewondo, Nerine; Garbin, Valeria; Pini, Ronny

DOI
10.1016/j.cherd.2023.02.014

Publication date
2023

Document Version
Final published version

Published in
Chemical Engineering Research and Design

Available online at www.sciencedirect.com

Chemical Engineering Research and Design

journal homepage: www.elsevier.com/locate/cherd

Experimental evidence of the effect of solute concentration on the collective evolution of bubbles in a regular pore-network

Nerine Joewondo[a], Valeria Garbin[a,b,*], Ronny Pini[a,**]

[a] Department of Chemical Engineering, Imperial College London, Exhibition Rd, London SW7 2AZ, United Kingdom
[b] Department of Chemical Engineering, Delft University of Technology, van der Maasweg 9, Delft 2629HZ, the Netherlands

ARTICLE INFO

Article history:
Received 13 December 2022
Received in revised form 12 February 2023
Accepted 13 February 2023
Available online 15 February 2023

Keywords:
Bubble dissolution
Porous media
Diffusive transport

ABSTRACT

The dissolution of bubbles confined in porous media is relevant to applications such as carbon sequestration and soil remediation. Recent numerical work indicates that a rich variety of collective dissolution behaviors can be obtained depending on the initial solute concentration, the size distribution of bubbles and the structure of the porous network. However, there is only sparse experimental evidence that supports these findings. Here, we present an experimental study that uses optical microscopy to track the dissolution of CO_2 bubbles in a two-dimensional porous network etched on a microfluidic chip filled with CO_2–saturated water. We consider two distinct level of initial liquid supersaturation for situations involving a single isolated bubble and small bubble clusters, and observe dissolution, growth or a combination of these processes. A pore-network model is used to complement the experimental observations with information on local concentration development. The model captures qualitatively the evolution of the bubble size in each case tested experimentally and enables shedding light on the interplay between the inter- and intra-pore diffusive fluxes in driving the dissolution process.

1. Introduction

The growth and dissolution of bubbles are important physical processes that occur in porous media. Relevant processes include the trapping of bubbles during subsurface storage of carbon dioxide (CO_2) (Alcalde et al., 2018; Macminn et al., 2010), soil remediation using microbubbles (Agarwal et al. (2016)) and the production of hydrocarbon reservoirs below their bubble point pressure (Gao et al. (2021)). For these applications, it is vital to resolve the fundamental mechanisms driving the dissolution of bubbles as a result of their interaction with the liquid phase.

The growth or dissolution of a gas bubble in a liquid results from a disequilibrium between the two phases, causing solute exchange between them (Ward et al., 1982; Makkonen and Vehmas, 2020; Epstein and Plesset, 1950). The diffusive flux through the curved gas-liquid interface is driven by the difference between the solute concentration in the liquid and its concentration at the interface. The latter is proportional to the Laplace pressure, which defines the difference

* Corresponding author at: Department of Chemical Engineering, Imperial College London, Exhibition Rd, London, SW7 2AZ, United Kingdom.
** Corresponding author.
E-mail addresses: v.garbin@tudelft.nl (V. Garbin), r.pini@imperial.ac.uk (R. Pini).
https://doi.org/10.1016/j.cherd.2023.02.014

between the pressure in the bubble and the pressure in the liquid (Epstein and Plesset, 1950; Duncan and Needham, 2004). The Laplace pressure is caused by surface tension, and for a spherical bubble, it is inversely proportional to its radius. A system containing bubbles of different sizes dispersed in a continuous liquid phase is thus characterized by multiple local surface concentrations (Ward et al. (1982)). To reach thermodynamic stability, this multi-bubble system must evolve to a configuration characterised by either an individual bubble or by multiple bubbles with equivalent curvature. Because the Laplace pressure drives by and large this transition, Ostwald ripening occurs, whereby larger bubbles grow at the expense of the smaller bubbles (Ostwald, 1897; Schmelzer and Schweitzer, 1987; Lifshitz and Slyozov, 1961). Yet, within such multi-bubble system, the evolution of individual bubbles is a complex process controlled by the interplay between the local solute transport through the gas/liquid interface and within the liquid. For instance, it has been shown through experimental and modelling work that the diffusive shielding caused by neighboring bubbles can delay and arrest the dissolution or growth of a densely populated bubble lattice (Weijs et al., 2012; Vega-Martínez et al., 2020; Laghezza et al., 2016; Michelin et al., 2018). As such, the dynamics of the growth/dissolution process depend strongly on the size of the bubble lattice (Weijs et al., 2012; Michelin et al., 2018), its spatial distribution (Weijs et al., 2012; Michelin et al., 2018), and the initial solute distribution in the liquid (Peñas-López et al., 2016; Soto et al., 2019).

In porous media, the local arrangement of pore throats and pore bodies complicates the process described above in at least two ways. First, the morphology of the pore space constrains the physical growth of the bubble, which can expand beyond the limits of the pore body into the adjacent pore throats (Chalendar et al., 2018; Xu et al., 2017; Li et al., 2020; Mehmani and Xu, 2022). Under these conditions, the controlling Laplace pressure is determined by the local interface curvature within the (small) pore throats, rather than by the size of the bubble itself. Situations can thus arise where smaller bubbles grow at the expense of larger bubbles (Chalendar et al., 2018; Xu et al., 2017) – opposite to the phenomenon of Ostwald ripening described above. Second, the tortuosity of the pore space limits diffusive mass transport relative to diffusion in bulk liquid (Weissberg (1963)). As a result, a multi-bubble system confined in porous media experiences enhanced diffusive shielding, whereby individual bubbles may undergo periods of growth and dissolution alternately (Joewondo et al. (2022)). However, experimental evidence of this effect has so far been lacking.

To address this knowledge gap, we present here experimental observations of the dissolution of individual CO_2 bubbles and small bubble clusters (2–4 bubbles) in a regular pore-network filled with CO_2–saturated water. In doing so, we consider similar systems reported in recent pore-scale modelling studies (Chalendar et al., 2018; Singh et al., 2022) and investigate the effects of initial supersaturation in the liquid phase and of initial bubble size. By comparing observations on bubble clusters with their individual counterparts, we provide experimental evidence on the effects of diffusive transport and local concentration development in driving dissolution, growth or a combination of these processes. To further support the experimental observations and to shed light on the underlying diffusive fluxes, we carry out a comparison with predictions obtained upon application of a pore-network model.

2. Theory

2.1. Saturation concentration

Given a planar gas-liquid interface, Henry's Law describes the solute concentration, C_s^0, of a liquid that is thermodynamically at equilibrium with the partial pressure of the gas phase at pressure P^0:

$$C_s^0 = k_H(T) M P^0 \tag{1}$$

where k_H is the Henry's constant and M is the molecular weight of the solute. The temperature dependence of the Henry's constant is described by the van't Hoff equation:

$$k_H(T) = k^*_H \exp\left[B\left(\frac{1}{T} - \frac{1}{T^*}\right)\right] \tag{2}$$

where k^*_H is the Henry's constant at the reference temperature $T^* = 298.15$ K, and B is the constant for each gas species. For CO_2, k^*_H and B are taken to be 3.3×10^{-4} mol · m^{-3} · Pa^{-1} and 2400 K (Sander (2015)).

2.2. Equilibrium considerations

The equilibrium condition of a single-component bubble in a liquid is described by the chemical potential of the solute in the liquid, μ^d, and the chemical potential of the the bubble, μ^b (Ward et al., 1982; Makkonen and Vehmas, 2020). The former is defined as follows:

$$\mu^d = \mu^0 + R_g T \ln(C^0/C_s^0) \tag{3}$$

where C^0 is the solute concentration in the liquid, μ^0 is the chemical potential of the pure solute and R_g is the universal gas constant (8.314 J · mol^{-1} · K^{-1}). The ratio of the solute concentration relative to the saturation concentration is referred to as the liquid saturation, $f = C^0/C_s^0$. The chemical potential of the bubble is defined as follows:

$$\mu^b = \mu^0 + R_g T \ln((P^0 + 2\gamma/R)/P^0) \tag{4}$$

where γ is the surface tension, R is the radius of the bubble and $2\gamma/R$ is the Laplace pressure. At thermodynamic equilibrium, $\mu^b = \mu^d$, yielding a relationship between the equilibrium liquid saturation f_{eq} and the equilibrium bubble radius, R_{eq}:

$$f_{eq} = 1 + \frac{2\gamma/R_{eq}}{P^0} \tag{5}$$

3. Experimental methodology

3.1. Experimental setup

Optical microscopy was used to monitor the dissolution of CO_2 bubbles in water within a transparent glass microfluidic chip. The 10 × 20 mm borosilicate glass chip was custom-designed to have a regular and uniform pore-network pattern (Micronit BV, Enschede, The Netherlands). The engraved pattern consists of 1313 cylindrical pore bodies of 148.5 μm radius and 20 μm height. Each pore body is connected to four neighbors by rectangular prisms (throats) with the following dimensions: 45 μm (width), 20 μm (height), 99 μm (length). The micromodel porosity and pore volume (PV) are 0.44 and 2×10^{-9} m^3, respectively.

The schematic of the full experimental setup is shown in Fig. 1a. CO_2 gas with 99.8 % purity (BOC Ltd., Woking, United

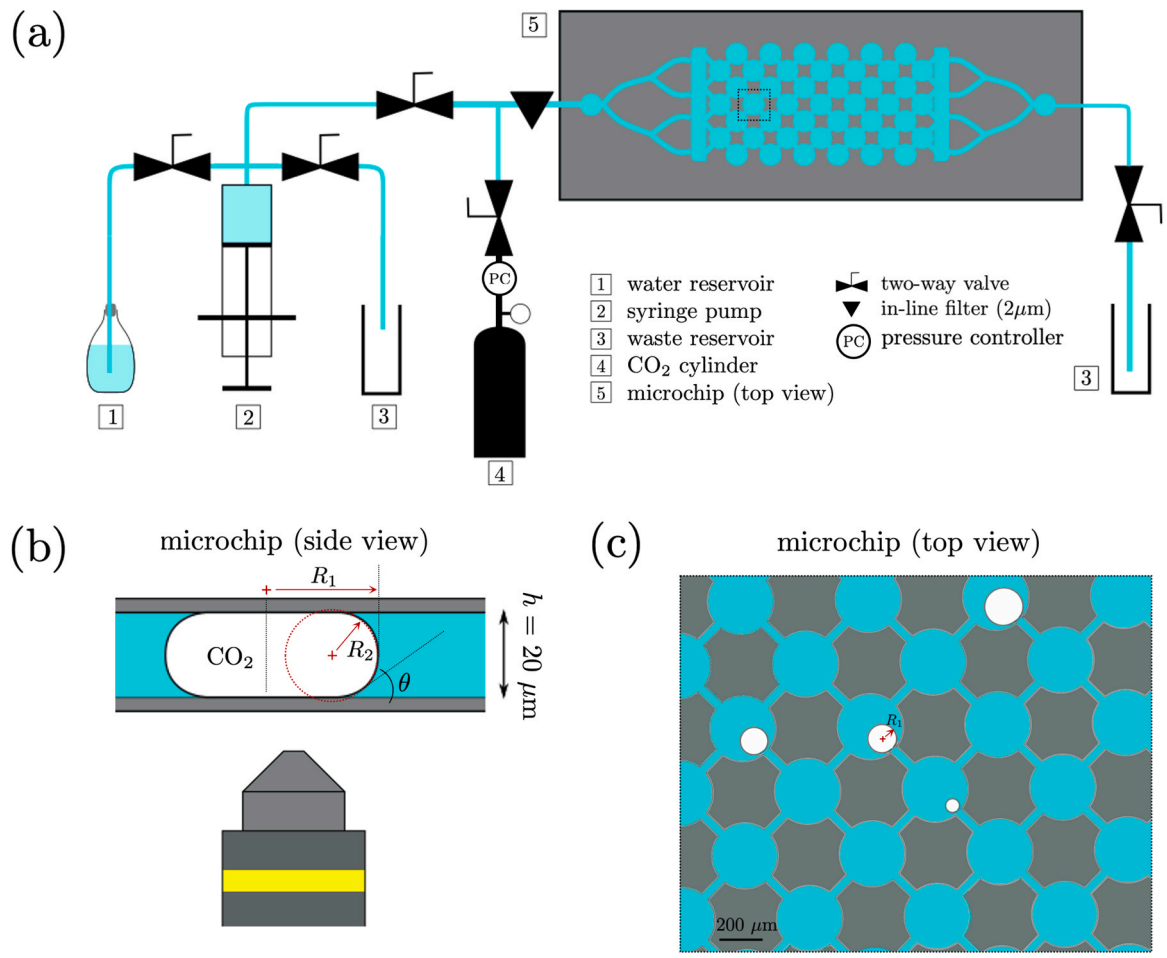

Fig. 1 – (a) The schematic of the experimental setup that consists of the microfluidic chip with a pore network pattern. The chip is connected to a water and a CO_2 reservoir (upstream) and a waste reservoir (downstream). Water injection is driven by a Teledyne 100D ISCO syringe pump, while the CO_2 injection is set by a pressure controller. The setup is completed by a 2 μm in-line filter mounted just prior the entrance of the micrfluidic chip, and by two-way valves fitted upstream and downstream of the system. During the experiment, the microfluidic chip is placed on the microscope stage. (b) Schematic of the side view of the microchip pore body containing a CO_2 bubble, characterized by two radii of curvature, namely the top view radius R_1 and the side view radius R_2. (c) An example of image collected during one experiment showing four CO_2 bubbles and their corresponding top view radius R_1.

Kingdom) was connected to the chip via a pressure controller (MFCS-EZ, Fluigent, Le Kremlin-Bicêtre, France). DI Water (18.2 MΩ cm) from Milli-Q purifying system was injected into the chip using a Teledyne 100D ISCO syringe pump via 1/16" OD ETFE tubing. A PEEK pre-column filter (2 μm) was fitted upstream of the microfluidic chip to prevent contamination. Two-way PEEK valves (P-732, IDEX Corp., Illinois, United States) mounted upstream and downstream of the microfluidic chip were used to isolate the system during the dissolution experiments. A type K thermocouple tip connected to a data-logger (TC-08, Pico Technology Ltd., United Kingdom) was placed on the top glass of the microfluidic chip to monitor the experimental temperature. Only experiments with a deviation ≤ 0.4 K in the measured experimental temperature were considered.

The inverted optical microscope Zeiss Axio Observer A 0.1 m (Carl Zeiss AG, Oberkochen, Germany) was used in combination with a programmable stage (MAC 6000, Ludl Electronic Products, Ltd., New York, United States), a CMOS (DCC1545M, Thorlabs, New Jersey, United States) camera, and a 5 × objective lens to capture monochrome images of the microfluidic chip with the size of 1280 × 1024 pixels (≈ 5 % pattern area containing 21 ± 3 pore bodies per image tile) resulting in the resolution of 1.62 μm/px. Fig. 1c shows an exemplary image of one section of the microfluidic chip filled with water and containing four CO_2 bubbles. Fig. 1b shows the expected side-view of one bubble resting in one cylindrical pore body. The effective radius of curvature of each bubble is estimated as $R = 2/(R_1^{-1} + (h/2/\cos\theta)^{-1})$, where R_1 is the measured top-view radius of the bubble, $h = 20\mu m$ is the height of the channel. The contact angle, θ, is taken to be 62° ± 7° as reported elsewhere for static CO_2 bubbles in a glass microchannel (Jafari and Jung (2017)). The bubble shape assumed in Fig. 1b is supported by the following argumentation. For $R_1 = 5 - 100\ \mu m$, and under the ambient conditions of our experiments, capillary forces are strong enough to prevent the bubble from detaching from the bottom surface of the micromodel due to buoyancy. In fact, $2\pi R_1(1 - cos\theta)\gamma >> \Delta\rho g\pi R_1^2 h$, where $\gamma = 0.0727$ N/m is the gas/liquid interfacial tension, $\Delta\rho \approx 1000\ kg/m^3$ is the density difference between the liquid and gas phase, and $g = 9.81\ m/s^2$ is the acceleration due to gravity.

3.2. Experimental procedure

Under the experimental conditions, the Henry's constant, the diffusion coefficient and the surface tension of the CO_2-water fluid pair take the following values: $k_H = 3.73 \times 10^{-4}$ mol · m^{-3} · Pa^{-1}; $D = 2.17 \times 10^{-9}$ m^2/s; $\gamma = 0.0727$ N/m. Two distinct sets of experiments were carried out to explore the effect of initial saturation on bubble evolution. In the first case, DI-water at $T_1 = 291.40 \pm 0.3$ K was used. In the second case, DI-water was cooled to a temperature of $T_1 = 287.15 \pm 0.5$ K, while bubbling CO_2 gas at 1 bar, before injecting it into the micromodel. In both cases, the liquid phase is oversaturated ($f^0 = k_H(T_1)/k_H(T_2) = 1.06$ and 1.20, respectively), because of the higher temperature maintained during the experiment (T_2 = 293.65 ± 0.4 K). Recordings of the experimental temperature (T_2) for each case and for the entire duration of the image acquisition process are provided a supplementary material.

The following sequence was used to inject the operating fluids (CO_2 and DI-water prepared as described above) in the microfluidic chip (downstream valve open) and to generate bubbles: .

1. water injection at a constant pressure of 2 bar for 10 min to saturate the microfluidic chip (flow rate 0.17–0.23 mL/min, corresponding to the injection of ≈ 968 ± 205 PV);
2. CO_2 injection at a constant pressure of 1 bar until gas breakthrough (approx. 1 min);
3. water injection at a constant pressure of 2 bar for 10–20 s (flow rate 0.17–0.23 mL/min, corresponding to the injection of ≈ 24 ± 10 PV);

After completing this sequence, the downstream valve connecting the microfluidic device to the waste reservoir was closed as soon as the pressure measured by the syringe pump read 1 bar. The microfluidic chip was isolated by closing the upstream valve, and from this point the in-situ pressure was not monitored. This procedure generated ~ 200 bubbles (i.e. ~ 15 % of the pore bodies contained a bubble), which were predominantly smaller than the size of a pore body. μManager software (Edelstein et al., 2010) was used to operate the programmable stage and the camera, so as to take images of different sections of the microfluidic chip. Images were recorded for up to 16 h at 20 s intervals. For further processing, images were selected manually based on the spatial distribution of the bubbles. To minimize potential boundary effects experienced by the bubbles, images were selected in the center of the microfluidic chip. To minimize contributions from surrounding bubbles, images were selected with up to four bubbles in a field containing 21 ± 3 pore bodies. At the end of each experiment, a background image of the water-filled microfluidic chip was acquired for background subtraction.

A total of eight experiments were conducted at a constant temperature of 293.65 K and a pressure of 1 bar to include the analysis of both isolated bubbles (Cases 1–4 in Table 1) and small bubble clusters (Cases 5–8, consisting of bubble pairs as well as clusters of up to 4 bubbles) As depicted in Fig. 2, the bubbles in these clusters are classified in terms of their distance to the smallest bubble. As such, an isolated bubble refers to a bubble with no immediate neighbors (1st–2nd degree neighbors, Case 1–4), and a bubble pair refers to two bubbles in adjacent pore bodies (1st degree neighbors, Case 7 and 8). A bubble cluster is formed when in addition to the bubble pair, 2nd and/or 3rd degree neighbors are present (Case 5 and 6).

3.3. Image processing and analysis

An image processing workflow was implemented in MATLAB R2021b and comprised of five steps. In the first step, the images were cropped to regions containing the bubbles to reduce processing time (the dataset containing the images is provided as Supplementary Material). In the second step, the background image was segmented into solid and pore spaces. To this end, a thresholding level based on Otsu's method was applied (function multitresh), followed by an area-opening operation (function bwareaopen) to flood-fill the solid space bounded by the liquid-solid outlines. The difference between 2D porosity derived from the segmented background image and the designed pattern was calculated to be ≤ 4 %. In the third step, any misalignment between each acquired image and the background image was detected by performing 2D convolution (function conv2) and corrected accordingly. In the fourth step, each image was segmented to identify bubbles and solid space by applying again a thresholding level based on Otsu's method. The channel outline was then eliminated from each image by subtracting the segmented background image. In the fifth step, the x- and y- coordinates of the interface of each bubble were extracted using the function bwboundaries. The bubble's in-plane radius, R_1, was then computed as $R_1 = \sqrt{A_b/\pi}$, where A_b is the bubble's in-plane area obtained using the function polyarea, which requires the x- and y- coordinates of the interface as input.

Processed images representing the initial condition in each experiment (Case 1–8) are shown in Fig. 3. For each case, the analysis focuses on the temporal evolution of the radius of the smallest bubble (highlighted with a red circle), as it more strongly manifests collective effects. The equilibrium saturation f_{eq} for each bubble and the equilibrium bubble radius R_{eq} for each initial saturation were calculated using Eq. (5). The ratio between the initial effective bubble radius and the equilibrium radius, R^0/R_{eq} classifies a bubble's initial equilibrium condition. Specifically, an isolated bubble can only be at equilibrium with its surroundings when $R^0/R_{eq} = 1$. For $R^0/R_{eq} > 1$ bubble growth is expected, while for $R^0/R_{eq} < 1$ the bubble is expected to dissolve.

4. Pore-network modelling

We utilized a pore-network model (PNM) derived in our previous work (Joewondo et al. (2022)) to support the analysis of the experiments. This model was developed to address limitations of PNMs reported in literature that lack the description of the interdependence between the temporal evolution of bubble radius and the dissolved solute distribution in the liquid. The network is made of spherical pore bodies of radius R_p connected to $N_t = 4$ adjacent pore bodies through straight cylindrical pore throats with cross-sectional area and length A_t and L_t, respectively. Each pore body can be occupied by up to one spherical bubble of radius $R \leq R_p$. Upon dissolution (or growth), the bubble's interface will retract (or advance), while the bubble remains stationary in the center of the pore body. The solute concentration within a given pore body, C_p, evolves in time due to mass exchange with the neighboring pore bodies and with the bubble residing in it.

Table 1 – Summary of the experiments conducted in this study. These differ in the value of the initial fluid saturation (f^0) and initial bubble radius (R_1^0 and R^0) relative to the their equilibrium counterparts (f_{eq} and R_{eq}). Values of the same properties used to initialize the pore-network simulations are also listed. Cases 1–4 involve isolated bubbles, while Cases 5–8 involve bubble-pairs.

		Experimental							Pore-network model			
			Main bubble			Neighbors				Main bubble		Neighbors
Case	R^0/R_{eq} [–]	f^0 [μm]	R_1^0 [μm]	R^0 [–]	f^0/f_{eq} [–]	distance	R_1^0 [μm]	R^0 [μm]	f^0 [–]	R^0 [μm]	f^0/f_{eq} [–]	R^0 [μm]
1	0.77	1.06	16.5	18.6	0.983	–	–	–	1.02	62.0	0.995	–
2	1.06	1.06	32.8	25.8	1.003	–	–	–	1.02	86.1	1.001	–
3	2.93	1.20	21.3	21.3	1.123	–	–	–	1.06	70.3	1.039	–
4	4.05	1.20	48.0	29.5	1.144	–	–	–	1.06	97.4	1.045	–
5	1.07	1.06	32.9	25.8	1.003	1st	113.4	35.9	1.02	86.2	1.001	119.5
						3rd	120.8	36.2				120.7
6	1.13	1.06	39.0	27.5	1.007	1st	93.6	34.7	1.02	91.8	1.002	115.7
						2nd	75.2	33.2				110.7
						3rd	108.9	35.6				118.8
7	3.57	1.20	33.2	26.0	1.136	1st	57.5	31.1	1.06	85.7	1.043	102.6
8	3.83	1.20	40.2	27.9	1.140	1st	65.9	32.2	1.06	91.9	1.044	106.3

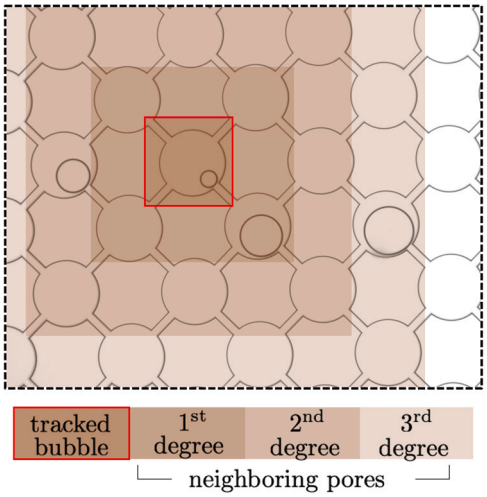

Fig. 2 – Exemplary field of view of the microfluidic chip during image acquisition of a bubble cluster consisting of four bubbles. These are classified in terms of their distance to the smallest bubble (highlighted with a red box). In this case the smallest bubble has one 1st degree, one 2nd degree and one 3rd degree neighbor.

Both processes are diffusive and their fluxes, J, are expressed by the one-dimensional form of Fick's first law. The flux between neighboring pore bodies n and i is:

$$J_{n\to i} = -\frac{D}{L_t}(C_{p,i} - C_{p,n}). \tag{6}$$

where D is the diffusion coefficient. The flux through the gas-liquid interface in pore body i is:

$$J_{b,i\to i} = -\frac{D}{R_i}(C_{p,i} - C_{s,i}). \tag{7}$$

The sign convention implies that solute uptake by the liquid phase within pore body i is characterized by a positive value of the flux. Accounting for these two diffusive processes, the temporal evolution of the solute concentration in a given pore body i that contains a bubble of radius R_i is described by the following differential equation:

$$\frac{dC_{p,i}}{dt} = -D\frac{A_t}{L_t\epsilon_i V_p}\sum_{j=1}^{N_t}(C_{p,i} - C_{p,j}) - \frac{4\pi R_i^2}{\epsilon_i V_p}\frac{dR_i}{dt}\left(\rho^0 + \frac{4M\gamma}{3R_g TR_i} - C_{p,i}\right). \tag{8}$$

where V_p is the volume of the pore body, $\epsilon_i = (V_p - 4\pi R_i^3/3)/V_p$ is the volume fraction of liquid in the pore body and $\rho^0 = P^0/R_gT$. The evolution of the bubble radius, dR_i/dt, was formulated following the Epstein & Plesset equation (Epstein and Plesset, 1950; Duncan and Needham, 2004):

$$\frac{dR_i}{dt} = D(C_{p,i} - C_{s,i})\left(\rho^0 + \frac{4M\gamma}{3R_g TR_i}\right)^{-1}\frac{1}{R_i} \tag{9}$$

where $C_{s,i} = k_H M(P^0 + 2\gamma/R_i)$.

For each experimental case, the bubbles considered in the PNM simulation are highlighted with a shaded area in Fig. 3. For each simulation, bubbles were located around the center of the network, and Eqs. (8) and (9) were solved using the ode45 solver in MATLAB for a network consisting 64 pore bodies. This number was deemed to be sufficient to avoid boundary effects. The pore-network model was parameterized using the values reported in Table 1. We note that R^0/R_{eq} for each simulated bubble (tracked and neighbors) was fixed at the experimental value, while letting the initial saturation, f^0, to differ slightly from the estimates based on the Henry's constants. Parameterizing the PNM in this way ensured that the initial conditions of each bubble relative to the equilibrium condition, which was assumed to control the bubble's qualitative behavior, were maintained. Yet, this parameterization results in different absolute values of the bubble radius in the PNM simulations and in the experiments, yielding different dissolution times. To qualitatively compare the simulation and behaviors observed experimentally, we normalized the timescale by the bubble's lifetime obtained in Case 1. We note that in Case 1, 2 and 3 only one bubble was simulated, despite a second bubble is visible in the micromodel. As indicated by the PNM simulations presented in Section S1 and S2 of the Supporting Information, the larger neighboring bubble in 3rd degree position has a negligible contribution to the evolution of the tracked bubble. Similarly, for Cases 7 and 8 including the 3rd degree

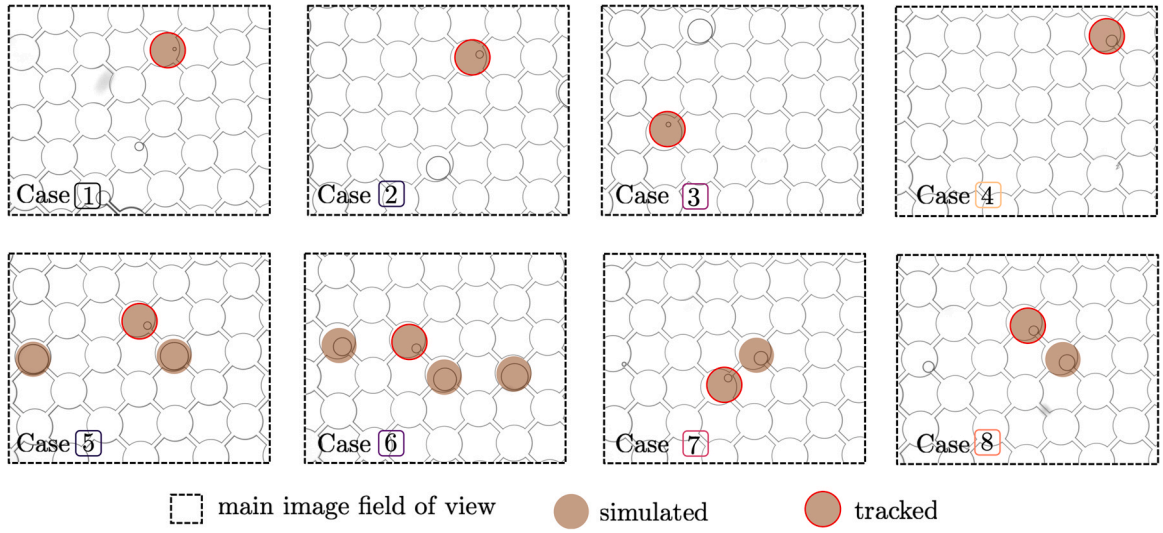

Fig. 3 – Initial condition for each experiment conducted in this study (Case 1–8 in Table 1). Each panel in the figure corresponds to one experiment and represents the field of view of the microfluidic chip during image acquisition. In each case, the smallest bubble is highlighted with a red circle and corresponds to the bubble considered for detailed analysis. Bubbles highlighted with a shaded area are considered in the pore-network simulation.

neighbor in the PNM simulation does not affect the evolution of the tracked bubble.

5. Results and discussion

5.1. *Experimental observations*

Figure 4a shows a state diagram, on which the equilibrium condition, Eq. (5), is plotted as a solid black line. The grey and white areas above and below this line represent conditions at which a bubble would grow and dissolve, respectively. The single markers indicate the initial state of the smallest bubble in each experiment (Case 1–8, Table 1). The error bars represent the variation resulting from the uncertainty in the value of the contact angle, θ, used to estimate the bubble's Laplace pressure. Cases 1–4 correspond to experiments with an isolated bubble, while in Case 5–8 small bubble clusters are considered. Based on this state diagram, only Case 1 should show bubble dissolution. For each case, the temporal evolution of the top-view radius, R_1, is presented in Fig. 4b (isolated bubbles) and Fig. 4c (bubble clusters). For the latter, only the radius of the smallest bubble in the cluster is shown. We note that, as expected, all larger bubbles in Cases 5–8 grew due to their lower surface concentration relative to the smaller bubbles. The evolution of each bubble presented in Fig. 4b (isolated bubbles) conforms with expectations based on the state diagram: when $R^0/R_{eq} < 1$ (Case 1) the bubble dissolves, while when $R^0/R_{eq} > 1$ (Case 2–4) the bubble grows. We note that despite sharing similar values of top-view radii, R_1, the location of the bubble on the state diagram and, accordingly, the value of R^0/R_{eq} vary largely for Case 1 and 3, because the their initial liquid saturation levels differ. The evolution of the smallest bubble in the cluster (Fig. 4c) is not uniquely controlled by its initial location in the state diagram. One the one hand, in Cases 7 and 8 bubble growth is observed, in agreement with the larger liquid supersaturation experienced by the bubble pair. On the other hand, Case 5 and 6 (weak supersaturation) show bubble dissolution, despite $R^0/R_{eq} > 1$, this being the result of Ostwald ripening. We note that in these two cases, the smallest bubble undergoes a period of growth, before dissolving, indicating that its evolution may be controlled by the balance between two diffusing fluxes (within the pore body and between two adjacent pore bodies, see Discussion in Section 5.3). Notably, the bubble in Case 2 (isolated bubble) and Case 5 (bubble pair) are practically identical (similar low

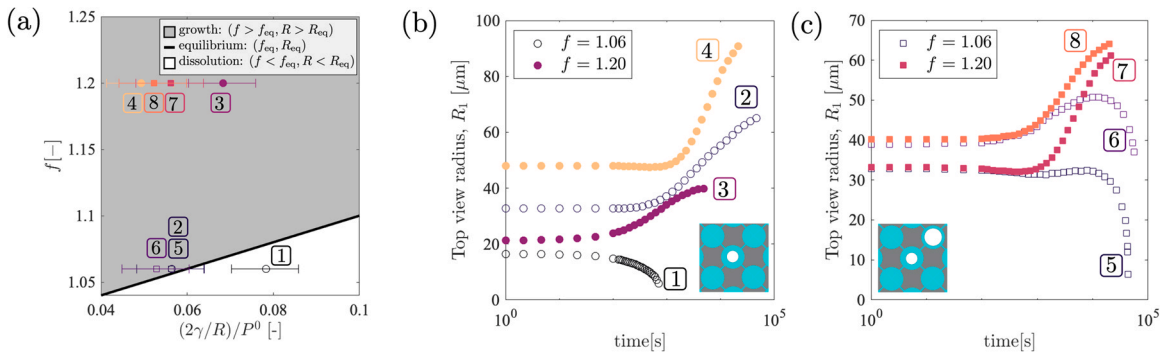

Fig. 4 – (a) Initial conditions of eight bubbles plotted on the equilibrium state diagram. The evolution of each bubble's top-view radius, R_1 is plotted against time for cases with (b) isolated bubbles and (c) bubbles with a larger neighboring bubble. The empty symbols refer to cases for $f = 1.06$ (weak supersaturation), while the filled symbols represent cases with $f = 1.20$ (strong supersaturation). The color-coding refer to each situation depicted in panels (b) and (c).

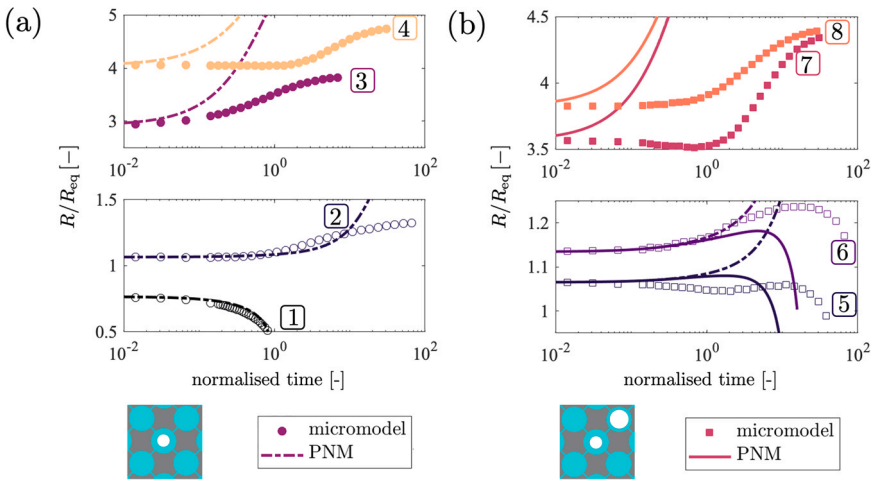

Fig. 5 – Comparison of the temporal evolution of the bubble's equivalent radius observed experimentally (symbols) with predictions obtained upon solving the pore-network model (lines) for cases involving (a) isolated bubbles and (b) bubble pairs. The bubble radius is normalized by R_{eq} while the time is normalized by the bubble's lifetime in Case 1. The empty symbols refer to cases for f = 1.06 (weak supersaturation), while the filled symbols represent cases with f = 1.20 (strong supersaturation).

oversaturation, R_1^0 = 32.8 and 32.9 μm). This fact confirms that the dissolution experienced by the smaller bubble in Case 5 is attributable to its interaction with the neighboring bubble.

5.2. *Ostwald ripening and non-monotonic evolution*

A qualitative comparison between the PNM simulations (solid lines) and the experimentally observed trends (symbols) is presented in Fig. 5a (isolated bubbles) and 5b (bubble clusters), this time in terms of the normalized radius R/R_{eq} as a function of the normalized time. For bubble clusters, an additional curve is shown (dotted line), which is the PNM prediction for an isolated bubble exposed to the exact same initial condition as in the bubble cluster. We note that the solid and dotted line overlap perfectly in Cases 7 and 8, because the tracked bubbles behave as isolated bubbles. It can be seen that the PNM correctly predicts the bubble evolution (dissolution or growth) in all cases, including the non-monotonic behavior observed for Case 5 and 6. In these two cases, the PNM simulations of the corresponding isolated bubbles show the expected growth of a bubble with $R/R_{eq} > 1$, confirming that the presence of larger neighboring bubble(s) can arrest the growth of a bubble and induce its dissolution (Ostwald ripening). Not surprisingly, the PNM predictions best match the experiments when the values of f^0/f_{eq} are also similar. As shown in Table 1, substantial differences are observed for Case 3, 4, 7 and 8, resulting in the PNM over-predicting bubble growth relative to the experimental observations. Importantly, in Case 6 the presence of 2nd and 3rd degree neighbors must be accounted for to correctly predict the evolution of the smallest bubble. As shown in Section S3 of the Supporting Information, simulations that consider only the nearest neighboring bubble predict bubble growth, indicating that the inter-pore fluxes generated by the presence of the additional bubbles contribute substantially to the dissolution process.

At this point, it is worth highlighting three major limitations of our PNM approach, which only allows for a qualitative comparison with the experiments. First, the geometries of the pore-bodies and pore-throats in the simulations and in the microfluidic chip differ substantially. The former assumes spherical bodies and cylindrical throats, while the micromodel consists of cylindrical bodies and rectangular throats. These affect the volumetric gas-liquid ratio in the system and gas-liquid interfacial area, effectively altering the rate of mass transfer. Second, bubbles observed experimentally were located near the solid wall as shown in Fig. 3 rather than in the center of the pore body, as assumed in the PNM. This discrepancy affects the effective distance between a bubble and its' neighboring pore bodies. Third, in our simulations we assume a uniform solute concentration within each pore body and an initial uniform concentration in the network. The former condition holds true when the time scale for bubble dissolution is much larger than that of solute diffusion across a pore body. As example, for Case 1 in Table 1 (the smallest bubble investigated) this ratio is approx. 9:1. Using the same argument, we expect that the approximation is valid even for a situation when a bubble is not located in the center of a pore body. However, the latter condition is difficult to validate in the absence of independent measurements of the solute concentration across the network.

5.3. *Competing diffusive fluxes using PNM*

The evolution of the bubbles's radius observed in the experiments is a macroscopic manifestation of the solute transport in the liquid phase, which in turns represents a balance between the solute flux through the gas-liquid interface and in the liquid. Due to the experimental limitations in acquiring real-time data of the solute's concentration field, the relevant fluxes can not be derived experimentally. Here, we exploit the PNM to derive these fluxes (Eqs. (6) and (7)) for Case 2 (isolated bubble) and 5 (bubble cluster). In these two cases the tracked bubble has similar initial bubble radii and saturation.

Figure 6a illustrates the directions of solute transport when pore body i contains a bubble that is smaller than the bubble located in the adjacent pore body (n1, 1st degree neighbor). Fig. 6b and c show the relevant fluxes for Case 2 and 5, respectively, including the flux through the bubble

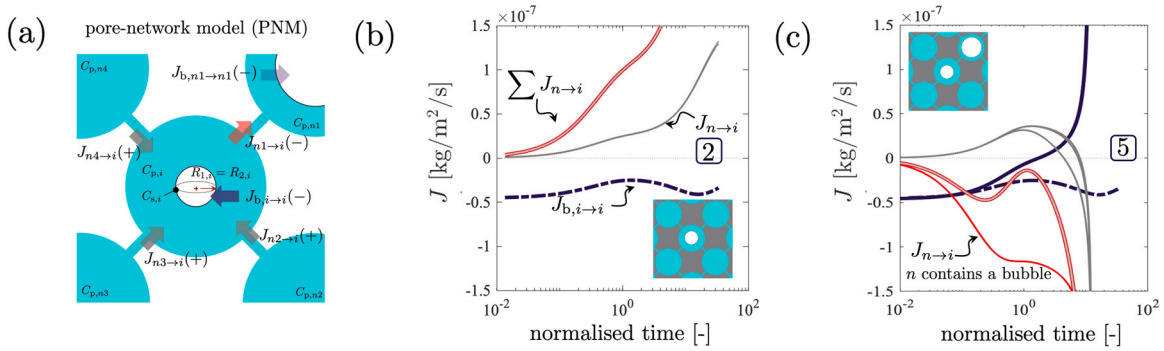

Fig. 6 – (a) Illustrative schematic of the solute fluxes that cause the growth of a bubble with a larger neighboring bubble, including both inter- and intra-pore fluxes. These fluxes are computed using the pore-network model for (b) Case 2 (isolated bubble) and (c) Case 5 (small bubble cluster). This plot also includes the flux of the isolate bubble for comparison (dashed line).

interface, $J_{b,i\to i}$, the flux in the liquid to each neighboring pore body, $J_{n\to i}$ and the total flux, $\sum J_{n\to i}$. A growing isolated bubble (Fig. 6b) uptakes solute from the pore body it resides in, triggering uptake from the empty neighboring pore bodies. This is evident from the negative values of $J_{b,i\to i}$ and the positive values of $\sum J_{n\to i}$. Such fluxes with opposing signs are expected when only one bubble influences the system, regardless of whether the bubble experiences growth or dissolution.

The presence of a larger 1st degree neighbor alters the evolution of the fluxes just described. In Fig. 6c we observe a transition point at normalized time ≈ 0.1, after which values of $J_{b,i\to i}$ for the bubble pair (solid line) deviate from the trend observed for the isolated bubble (dashed line). This transition is preceded by negative values of $\sum J_{n\to i}$ due to the solute uptake by the pore body containing the larger bubble. The flux $J_{n\to i}$ from the neighbor containing the larger bubble (red) differs from the fluxes towards the other empty neighboring pore bodies (grey). It is the balance of these fluxes over time that controls the evolution of the bubble in pore body i. We also note that in Fig. 6c the fluxes $J_{b,i\to i}$ of the isolated bubble and of the bubble pair diverge earlier (normalized time ≈ 0.1) than the corresponding radius-time curves (Fig. 5c, normalized time ≈ 0.5), suggesting that the latter arises as a consequence of the former.

6. Conclusions

We have presented and discussed experimental observations of the dissolution of individual CO_2 bubbles and small bubble clusters in a microfluidic 2D porous network visualized by optical microscopy. The experiments were conducted at two distinct levels of initial liquid supersaturation. For an isolated individual bubble, the equilibrium condition that accounts for the Laplace pressure is sufficient to predict whether the bubble will grow or dissolve. For a bubble cluster, this condition is not sufficient, because of the phenomenon of Ostwald ripening. Moreover, the interplay between the underlying diffusion fluxes (within the body and between neighboring pore bodies) may give rise to complex behaviors, in which the bubble undergoes periods of growth and dissolution alternately.

The lack of direct measurements of the evolving spatial solute concentration field within the liquid phase limits the extent to which the experiments can be interpreted. To address this limitation, we have complemented the experiments with pore-network model simulations. Despite its simplistic nature, the model was able to reproduce qualitatively the behaviours observed experimentally. Once parameterized, the model was used to compute both intra- and inter-pore diffusive fluxes, thus providing a complete picture of the mechanisms at play. The findings of this work highlight the role of solute transport in controlling the interactions between bubbles, and thus the need to develop experimental means to track the dissolved concentration in space and time. Recent experimental developments applied to a system comprising of a single bubble may enable to fill this gap (Peñas-López et al., 2015; Kong et al., 2018), if extended to systems involving pore-networks and multiple bubbles.

Data Availability

Data collected by optical microscopy and the temperature logs of each experimental case presented in this study are available through the Imperial Data Repository at https://doi.org/10.14469/hpc/12257(link embargoed until publication).

Declaration of Competing Interest

The authors declare that they have no known competing financial interests or personal relationships that could have appeared to influence the work reported in this paper.

Acknowledgments

NJ is funded by the Marit Mohn Scholarship at the Department of Chemical Engineering, Imperial College London.

Appendix A. Supporting information

Supplementary data associated with this article can be found in the online version at doi:10.1016/j.cherd.2023.02.014.

References

Agarwal, A., Zhou, Y., Liu, Y., 2016. Remediation of oil-contaminated sand with self-collapsing air microbubbles. Environ. Sci. Pollut. Res. 23 (23), 23876–23883.

Alcalde, J., Flude, S., Wilkinson, M., Johnson, G., Edlmann, K., Bond, C.E., Scott, V., Gilfillan, S.M., Ogaya, X., Haszeldine, R.S., et al., 2018. Estimating geological CO_2 Storage Security to

deliver on climate mitigation. Nat. Commun. 9 (1). https://doi.org/10.1038/s41467-018-04423-1
Chalendar, J.A.D., Garing, C., Benson, S.M., 2018. Pore-scale modelling of Ostwald ripening. J. Fluid Mech. 835, 363–392. https://doi.org/10.1017/jfm.2017.720
Duncan, P.B., Needham, D., 2004. Test of the Epstein-Plesset model for gas microparticle dissolution in aqueous media: effect of surface tension and gas undersaturation in solution. Langmuir 20 (7), 2567–2578. https://doi.org/10.1021/la034930i
Edelstein, A., Amodaj, N., Hoover, K., Vale, R., Stuurman, N., 2010. Computer control of microscopes using μ manager. Curr. Protoc. Mol. Biol. 92 (1). https://doi.org/10.1002/0471142727.mb1420s92
Epstein, P.S., Plesset, M.S., 1950. On the stability of gas bubbles in liquid-gas solutions. J. Chem. Phys. 18 (11), 1505–1509. https://doi.org/10.1063/1.1747520
Gao, Y., Georgiadis, A., Brussee, N., Coorn, A., van der Linde, H., Dietderich, J., Alpak, F.O., Eriksen, D., Mooijer-van denHeuvel, M., Appel, M., Sorop, T., Wilson, O.B., Berg, S., 2021. Capillarity and phase-mobility of a hydrocarbon gas-liquid system. Capillarity Porous Media.: Recent Adv. Chall. 76 (43).
Jafari, M., Jung, J., 2017. Direct measurement of static and dynamic contact angles using a random micromodel considering geological CO_2 Sequestration. Sustainability 9 (12), 2352. https://doi.org/10.3390/su9122352
Joewondo, N., Garbin, V., Pini, R., 2022. Nonuniform collective dissolution of bubbles in regular pore networks. Transp. Porous Media 141 (3), 649–666. https://doi.org/10.1007/s11242-021-01740-w
Kong, G., Buist, K., Peters, E., Kuipers, J., 2018. Dual emission LIF technique for pH and concentration field measurement around a rising bubble. Exp. Therm. Fluid Sci. 93, 186–194.
Laghezza, G., Dietrich, E., Yeomans, J.M., Ledesma-Aguilar, R., Kooij, E.S., Zandvliet, H.J., Lohse, D., 2016. Collective and convective effects compete in patterns of dissolving surface droplets. Soft Matter 12 (26), 5787–5796. https://doi.org/10.1039/c6sm00767h
Li, Y., Garing, C., Benson, S.M., 2020. A continuum-scale representation of Ostwald ripening in heterogeneous porous media. J. Fluid Mech. 889, A14. https://doi.org/10.1017/jfm.2020.53
Lifshitz, I., Slyozov, V.V., 1961. The kinetics of precipitation from supersaturated solid solutions. J. Phys. Chem. Solids 19 (1), 35–50.
Macminn, C.W., Szulczewski, M.L., Juanes, R., 2010. CO_2 migration in saline aquifers. Part 1. Capillary trapping under slope and groundwater flow. J. Fluid Mech. 662, 329–351. https://doi.org/10.1017/S0022112010003319
Makkonen, L., Vehmas, T., 2020. Comment on "on the thermodynamic stability of bubbles, immiscible droplets, and cavities" by G. S. Manning. Phys. Chem. Chem. Phys. 23 (2021) 12490-12492. Phys. Chem. Chem. Phys. 22, 17523. https://doi.org/10.1039/D1CP01122G
Mehmani, Y., Xu, K., 2022. Capillary equilibration of trapped ganglia in porous media: a pore-network modeling approach. Adv. Water Resour. 166, 104223. https://doi.org/10.1016/j.advwatres.2022.104223
Michelin, S., Guérin, E., Lauga, E., 2018. Collective dissolution of microbubbles. Phys. Rev. Fluids 3 (4), 1–35. https://doi.org/10.1103/PhysRevFluids.3.043601
Ostwald, W., 1897. Studien über die Bildung und Umwaldlung fester Körper. Phys. Chem. 22, 289–330.
Peñas-López, P., Parrales, M.A., Rodríguez-Rodríguez, J., 2015. Dissolution of a CO_2 spherical cap bubble adhered to a flat surface in air-saturated water. J. Fluid Mech. 775, 53–76. https://doi.org/10.1017/jfm.2015.291
Peñas-López, P., Parrales, M.A., Rodríguez-Rodríguez, J., Van Der Meer, D., 2016. The history effect in bubble growth and dissolution. part 1. theory. J. Fluid Mech. 800, 180–212.
Sander, R., 2015. Compilation of Henry's law constants (version 4.0) for water as solvent. Atmos. Chem. Phys. 15 (8), 4399–4981. https://doi.org/10.5194/acp-15-4399-2015
Schmelzer, J., Schweitzer, F., 1987. Ostwald ripening of bubbles in liquid-gas solutions. J. Non-Equilib. Thermodyn. 12, 255–270. https://doi.org/10.1097/00000539-200205000-00027
Singh, D., Friis, H.A., Jettestuen, E., Helland, J.O., 2022. A level set approach to Ostwald ripening of trapped gas bubbles in porous media. Transp. Porous Media 145 (2), 441–474.
Soto, A.M., Enríquez, O.R., Prosperetti, A., Lohse, D., Van Der Meer, D., 2019. Transition to convection in single bubble diffusive growth. J. Fluid Mech. 871, 332–349.
Vega-Martínez, P., Rodríguez-Rodríguez, J., van der Meer, D., 2020. Growth of a bubble cloud in CO_2-saturated water under microgravity. Soft Matter 16, 4728–4738. https://doi.org/10.1039/D0SM00015A
Ward, C.A., Tikuisis, P., Venter, R.D., 1982. Stability of bubbles in a closed volume of liquid-gas solution. J. Appl. Phys. 53 (9), 6076–6084. https://doi.org/10.1063/1.331559
Weijs, J.H., Seddon, J.R.T., Lohse, D., 2012. Diffusive shielding stabilizes bulk nanobubble clusters. ChemPhysChem 13 (8), 2197–2204. https://doi.org/10.1002/cphc.201100807
Weissberg, H.L., 1963. Effective diffusion coefficient in porous media. J. Appl. Phys. 34 (9), 2636–2639.
Xu, K., Bonnecaze, R., Balhoff, M., 2017. Egalitarianism among bubbles in porous media: an ostwald ripening derived anticoarsening phenomenon. Phys. Rev. Lett. 119, 264502. https://doi.org/10.1103/PhysRevLett.119.264502